Framework for analyzing the thermoreflectance spectra of metal thermal transducers with spectrally tunable time-domain thermoreflectance

Framework for analyzing the thermoreflectance spectra of metal thermal transducers with spectrally-tunable time-domain thermoreflectance

Liang Zhang,[1, #] Weiqiang Li,[1, 2, #] Lenan Zhang,[3, #] Yang Zhong,[3] Xiao Guo,[1, 2] Long Li,[1] Evelyn N. Wang,[3, a), *] and Liang Guo [1, a), *]

AFFILIATIONS

[1]Department of Mechanical and Energy Engineering, Southern University of Science and Technology, Shenzhen, 518055, China

[2]Department of Mechatronics Engineering, Harbin Institute of Technology, Harbin, 150001, China

[3]Device Research Laboratory, Department of Mechanical Engineering, Massachusetts Institute of Technology, 77 Massachusetts Avenue, Cambridge, Massachusetts 02139, USA

[a)]**Authors to whom correspondence should be addressed:** enwang@mit.edu and guol3@sustech.edu.cn

# These authors contribute equally to this work.

* Corresponding authors at Device Research Laboratory, Department of Mechanical Engineering, Massachusetts Institute of Technology, 77 Massachusetts Avenue, Cambridge, Massachusetts 02139, USA and Department of Mechanical and Energy Engineering, Southern University of Science and Technology, Shenzhen, 518055, China.

ABSTRACT

The time-domain thermoreflectance (TDTR) technique has been widely used to measure thermal properties. The design and interpretation of TDTR experiment rely on an in-depth understanding of the thermoreflectance signature for a given metal thermal transducer. Although the TDTR signals of several metal thermal transducers have been experimentally investigated, a practical framework bridging the electronic properties and the thermoreflectance characteristics of metal thermal transducers will be helpful for future study. Compiling published results and our analysis and tests, in this work, we show a theoretical strategy to determine the thermally-induced change of reflectance spectra with the electronic properties of metal transducers as the input. As a natural consequence of the proposed framework, we show that the optimal probe photon energy occurs near the interband transition threshold (ITT) of the metal. To validate our approach, TDTR experiments are performed with Au and Cu as two representative metal thermal transducers in two temporal regimes when electrons and lattice have different temperatures (<10 ps) and reach thermal equilibrium (>10 ps), respectively. The experimental results show good agreement with the theory. The work fundamentally elucidates the thermally-induced optical response of metal thermal transducers, and also provides practical guidelines for choosing the appropriate probe photon energy to optimize the TDTR signal for a given metal thermal transducer, which is useful for broadening the adaptability of TDTR to various experimental conditions, materials, and new laser sources.

I. INTRODUCTION

Characterizing thermal properties, such as thermal conductivity and interface thermal resistance, is of significant interest in both fundamental studies and practical applications[1-4]. Compared with traditional contact methods for measuring thermal properties based on resistance heating/sensing or thermocouple, time-domain thermoreflectance (TDTR) is particularly important for micro-to-nanoscale thermal transport study due to its high-spatial resolution and noninvasive nature. In a typical TDTR measurement, laser pulses from an ultrafast laser are used for heating (i. e., pump) and sensing (i. e., probe). The pump pulse first reaches the sample and induces a temperature rise. Then, the probe pulse arrives with an adjustable time delay and detects the temperature evolution from the change of reflectance. To realize sufficient

sensitivity to the temperature change and high accuracy of the thermal property measurements, a thin metal film as a thermal transducer is coated on the sample, the reflectance change of which is linear versus temperature change when the heating is perturbative. For a conventional TDTR setup, a Ti: sapphire femtosecond laser is commonly used, which provides near-800 nm probe wavelength (1.55 eV). Since the reflectance of Al near 1.55 eV is sensitive to temperature change, the "1.55 eV probe + Al" has been the most popular combination for TDTR measurements[5-10] (NbV, Pt, Ta, etc. are also used although rarely). However, this combination shows limitations on numerous scenarios. For example, Al does not perform well in high-temperature measurements due to oxidation or melting. In addition, since there is an increasing number of commercial laser sources featured by different photon energies, it is necessary to find alternative metal thermal transducers besides Al to broaden the adaptability of TDTR to various laser sources. For example, the wavelength of the femtosecond laser based on Yb-doped gain medium, which recently becomes popular due to the low cost and stable performance, is near 1030 nm (1.2 eV). However, Al is an improper thermal transducer for such laser sources due to insufficient sensitivity at 1.2 eV.

Previous studies have shown great potential to use different laser photon energies and metal thermal transducers in TDTR for thermal property measurements.The measured thermoreflectance spectra of a set of metals have been summrized[11-13], suggesting the possibility of using various metals as long as the corresponding optimal probe photon energy can be reached. Gengler *et al*. introduced an optical parametric oscillator (OPO) into a TDTR system to create a spectrally-tunable probe and demonstrated its adaptability to three different metal thermal transducers, Ti, Al, and Cu[14]. However, the optimization strategy for the TDTR signal relies on empirical knowledge since these works did not provide a detailed theoretical treatment for quantitatively predicting the thermoreflectance spectra and matching metal thermal transducers with proper probe photon energies. On the other hand, although the TDTR signals have been theoretically and experimentally interpreted to understand the electron-lattice coupling of metals in previous studies[15, 16], these works mainly focused on the nonequilibrium temporal regime within about 10 ps. Therefore, there still lacks a comprehensive framework considering more detailed electronic properties to guide TDTR measurements in the temporal regime later than 10 ps after electrons and lattice reach equilibrium.

This work elucidates the principle of matching metal thermal transducers and probe photon energies. A theoretical strategy, which accounts for the contributions of both electronic intraband and interband transitions, is developed to predict the thermoreflectance spectrum for a given metal thermal transducer. As an example, we calculate the thermoreflectance spectra for both Au and Cu, taking either the experimentally determined or predicted electronic band structure by first-principles calculation (Appendix A Table I) as the input. We use Au as the first example because Au has been widely studied previously and thus is an ideal validation for the proposed framework. On the other hand, Cu is chosen as it remains less investigated compared with Au. The insights gained from the present analysis can be useful for Cu-based TDTR measurements in the future. The spectrally-tunable TDTR system is enabled by an optical parametric amplifier (OPA) through optical nonlinear processes. With this system, we experimentally validate the theoretical prediction by measuring the thermoreflectance spectra of Au and Cu in both the nonequilibrium temporal regime (<10 ps) and equilibrium temporal regime (>10 ps), and good agreement with the theory is shown. The insights gained from our study provide a clear physical picture for the photothermics of metals and can serve as practical guidelines for optimizing the signal of TDTR systems deploying various laser sources or spectrally-tunable modules.

Ⅱ. THEORETICAL ANALYSIS OF THERMOREFLECTANCE

In TDTR measurements, a high sensitivity of reflectance to temperature change, i.e., a high value of $\Delta R/\Delta T$, is favored, where R and T denote reflectance and temperature, respectively. Therefore, theoretical analysis of the thermoreflectance spectra of various metals is instructive for choosing the correct metal thermal transducer given a probe photon energy and vice versa. Figure 1 shows the overall theoretical framework for the thermoreflectance spectrum calculation, from which the key role of the frequency (ω)- and electron temperature (T_e)-dependent dielectric constant $\varepsilon(\omega, T_e)$ is manifested. The refractive index n is simply the square root of the dielectric constant, based on which the reflectance can be derived from the Fresnel equations.

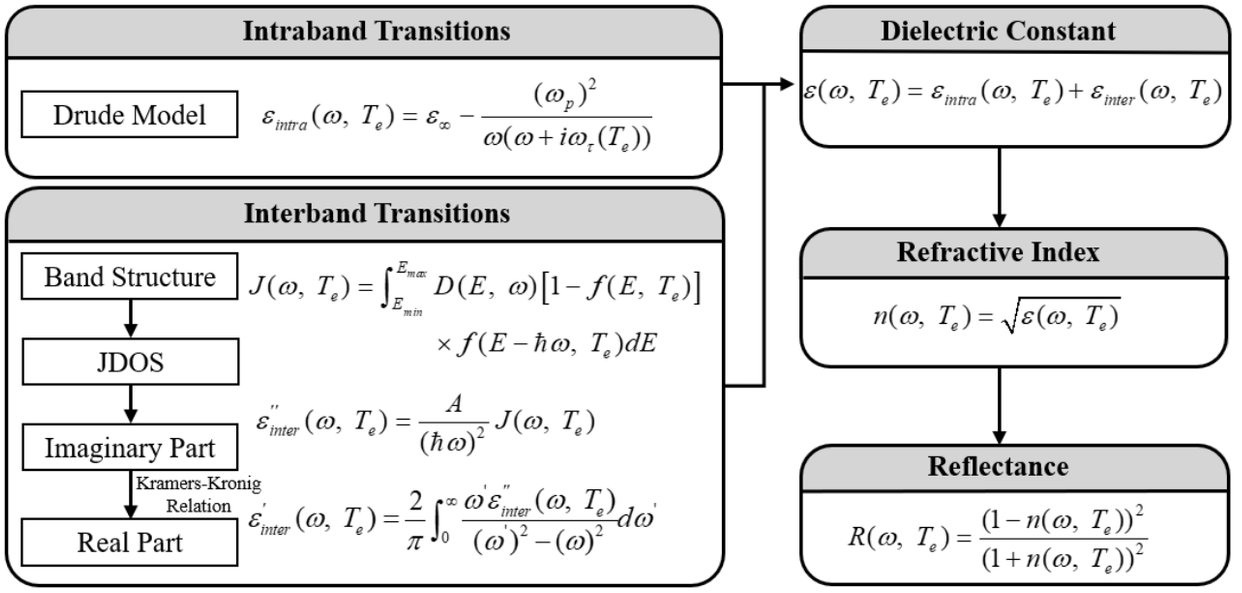

FIG. 1. Theoretical framework of the thermoreflectance spectrum calculation. Two parts of contributions should be considered in the calculation of the dielectric constant: intraband transitions and interband transitions. Intraband transitions can be depicted by Drude model, and interband transitions can be calculated through joint density of state (JDOS). Reflectance can be calculated with Fresnel equation from refractive index which is the square root of the dielectric constant.

The thermally-induced change of reflectance can be obtained through the following perturbative expansion:

$$\frac{\Delta R}{R} = \frac{1}{R}\frac{\partial R}{\partial \varepsilon'}\Delta\varepsilon' + \frac{1}{R}\frac{\partial R}{\partial \varepsilon''}\Delta\varepsilon'' \tag{1}$$

where R, ε' and ε'' represent the reflectance, the real and the imaginary part of the dielectric constant, respectively. Following the stepwise relation from the dielectric constant to the refractive index to the reflectance, the expansion coefficients can be derived with the chain rule in differentiation:

$$\frac{\partial R}{R\partial \varepsilon'} = \frac{\partial R}{R\partial n'}\frac{\partial n'}{\partial \varepsilon'} + \frac{\partial R}{R\partial n''}\frac{\partial n''}{\partial \varepsilon'} = \frac{\sqrt{2(\varepsilon' + |\varepsilon|)}}{|\varepsilon|(|\varepsilon|^2 - 2\varepsilon' + 1)}(2\varepsilon' - |\varepsilon| - 1) \tag{2}$$

$$\frac{\partial R}{R\partial \varepsilon''} = \frac{\partial R}{R\partial n'}\frac{\partial n'}{\partial \varepsilon''} + \frac{\partial R}{R\partial n''}\frac{\partial n''}{\partial \varepsilon''} = \frac{\sqrt{2}\varepsilon''(2\varepsilon' + |\varepsilon| - 1)}{|\varepsilon|(|\varepsilon|^2 - 2\varepsilon' + 1)\sqrt{\varepsilon' + |\varepsilon|}} \tag{3}$$

where $|\varepsilon|$, n', and n'' are the norm of the dielectric constant, the real and the imaginary parts of the refravtive index, respectively.

The dielectric constant of metals includes contribution from both intraband and interband transitions

of electrons. In this work, we use Au and Cu for illustration as examples, because they have similar band structures and can represent the band structures of many other metals. As shown in Fig. 2, when the excitation photon energy is smaller than the ITT, only intraband transitions of free electrons in the *s*/*p* band contribute to the dielectric constant, which can be described by the Drude model[17]. When the excitation photon energy is larger than the ITT, electrons in the *d* band can be excited into states in the *s*/*p* band above the Fermi level (E_F), which is determined by the band structure and the Fermi-Dirac distribution function. Combining the contribution from intraband (ε_{intra}) and interband (ε_{inter}) transitions, the total dielectric constant is given by

$$\varepsilon(\omega,\ T_e) = \varepsilon_{intra}(\omega,\ T_e) + \varepsilon_{inter}(\omega,\ T_e) \tag{4}$$

Similarly, the change of the dielectric constant also includes two parts of contribution

$$\Delta\varepsilon'(\omega,\ T_e) = \Delta\varepsilon'_{intra}(\omega,\ T_e) + \Delta\varepsilon'_{inter}(\omega,\ T_e) \tag{5}$$

$$\Delta\varepsilon''(\omega,\ T_e) = \Delta\varepsilon''_{intra}(\omega,\ T_e) + \Delta\varepsilon''_{inter}(\omega,\ T_e) \tag{6}$$

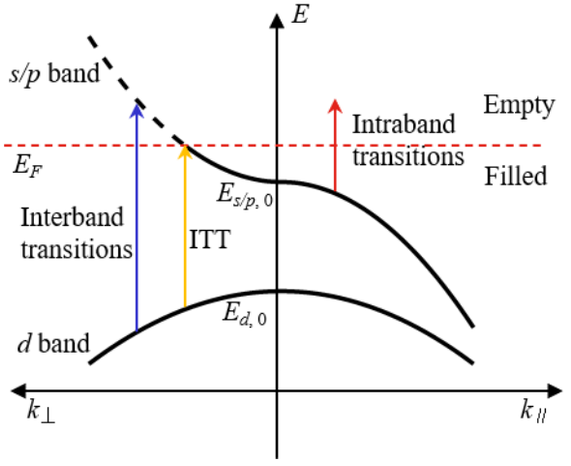

FIG. 2. Schematic showing landscape of optical transitions in Au and Cu (applied for metals with similar band structures). *d* band is full of electrons while *s*/*p* band is half full of electrons. The yellow line represents that an electron on the *d* band absorbs a photon with energy equal to the ITT, and transitions to Fermi energy level. The red line denotes that an electron on *s*/*p* band absorbs a photon with energy smaller than the ITT, and transitions to an energy level above the Fermi energy level, which is called intraband transitions. The blue line means an electron on *d* band absorbs a photon with energy larger

than the ITT, and transitions to *s/p* band above the Fermi energy level, which is called interband transitions.

A. Intraband Transitions

The Drude model is used to calculate the contribution due to intraband transitions of free electrons in the *s*/*p* band, which is given by

$$\varepsilon_{intra}(\omega,\ T_e) = \varepsilon_\infty - \frac{(\omega_p)^2}{\omega(\omega + i\omega_\tau(T_e))} \tag{7}$$

where ω and ω_p (1.37×10^{16} rad/s for Au[18] and 1.32×10^{16} rad/s for Cu[19]) are the light frequency and the plasma frequency, respectively. ε_∞ (4 for Au and 3 for Cu determined from fitting) describes the additional polarization due to the highly polarized environment caused by the filled *d* band close to the Fermi level[17]. ω_τ is the electron collision frequency, which is linearly dependent on electron temperature when eletrons and lattice are at thermal equilibrium,

$$\omega_\tau(T_e) = \alpha T_e \tag{8}$$

where α = 3.6×10^{11} rad/(sK) for Au[20] and 4.9×10^{11} rad/(sK) for Cu[21].

B. Interband Transitions

The imaginary part of the dielectric constant due to interband transitions ε''_{inter} is determined by the joint density of states $J(\omega, T_e)$ (JDOS)[22],

$$\varepsilon''_{inter}(\omega,\ T_e) = \frac{A}{(\hbar\omega)^2} J(\omega,\ T_e) \tag{9}$$

where *A* is a material-dependent constant determined by fitting with the measured dielectric constant (2.4 J^3m^3 for Au and 1.1 J^3m^3 for Cu). The contribution to the dielectric constant mainly comes from the high-symmetry points in the reciprocal space (L point and X point for Au and Cu). $\hbar$ is the reduced Planck's constant. Physically, the JDOS describes the number density of the possible electronic transitions from the *d* band to the *s*/*p* band, which is determined by the energy distribution of the JDOS (EDJDOS), $D(E, \omega)$ and the Fermi-Dirac distribution $f(E, T_e)$ through the integration with respect to energy *E*,

$$J(\omega, T_e) = \int_{E_{min}}^{E_{max}} D(E, \omega)[1 - f(E, T_e)] \times f(E - \hbar\omega, T_e) dE \quad (10)$$

$D(E, \omega)$ is given by the electronic structure of the *d* band and the *s*/*p* band:

$$D(E, \omega) = \frac{2}{(2\pi)^3} \int \frac{dl_{s/p,d}}{\left|\nabla_{\boldsymbol{k}}(E_{s/p}) \times \nabla_{\boldsymbol{k}}(E_d)\right|} \quad (11)$$

where $l_{s/p, d}$ denotes the integral path in the reciprocal space. $E_{s/p}$ and E_d are the energy in the *d* band and the *s*/*p* band, respectively. $\nabla_{\boldsymbol{k}}$ is the gradient with respect to the wave vector $\boldsymbol{k}$. Essentially, Eqs. (10) and (11) reveal that when the unoccupied upper band and the occupied lower band are parallel within a region in the reciprocal space and are separated by a energy difference ħω, the transition caused by absorption of a photon with energy ħω has a large probability of occurrence. The integration limits E_{min} and E_{max} in Eq. (10) should be carefully selected to avoid a singular point, which is given in Appendix A together with the detailed procedure of calculating the JDOS. The real part ε'_{inter} of the dielectric constant can be calculated from ε''_{inter} based on the Kramers-Kronig relation[23].

C. Theoretical Results of Thermoreflectance

Figure 3 shows the dielectric constant ((a), (c) for the real part and (b), (d) for the imaginary part) as a function of photon energy for both Au and Cu at 300 K. When the photon energy is smaller than the ITT (2.47 eV for Au[24] and 2.15 eV for Cu[25]), intraband transitions dominate the contribution to the dielectric constant. When the photon energy exceeds the ITT, both intraband and interband transitions need to be considered in order to fit well the experimental data. This is better manifested in the imaginary part, which directly reflects absorption strength. As shown in Fig. 3 (b) and (d), the imaginary part shartly increases when the photon energy exceeds the ITT since absorption due to interband transitions becomes allowed. In the calculation, the band structure parameters of Au are taken from Ref. 26 while the band structure parameters of Cu are computed using density functional theory, which are listed in Appendix A Table I. The theoretically calculated dielectric constant and the experimental data from Ref. 27 are consistent with each other as shown in Fig. 3. This fitting facilitates the determination of the coefficient *A* in Eq. (9).

With the contribution from both intraband and interband transitions quantified, Eqs. (1) to (3) can be used to calculate the thermally-induced reflectance change. The relative reflectance change $\Delta R/R$ of Au

and Cu for three temperature changes are illustrated in Fig. 4(a) and 4(b), respectively. Notably, the proportion constants for Au and Cu in Eq. (8) are cited or derived from literatures and do not have universally accepted values. We find that the utilization of the cited or derived values largely overestimates the influence of temperature on reflectance from the contribution of intraband transitions as shown in Appendix B. In fact, the contribution from interband transitions dominates the thermally-induced change of reflectance according to the experiment results introduced in Section III. Therefore, the relative reflectance change in Fig. 4 (and later in Fig. 6 and 7) is calculated based on only the contribution from interband transitions.

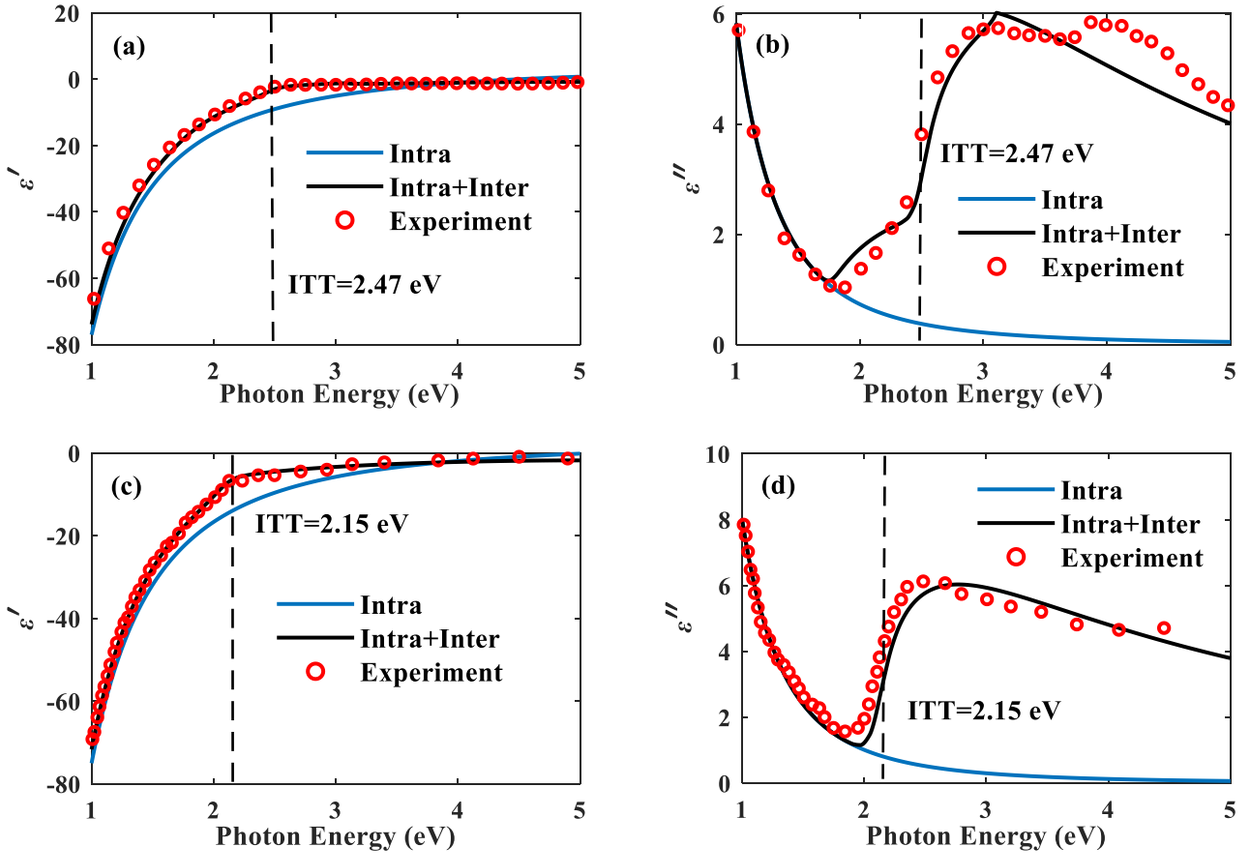

FIG. 3. Calculation results of (a) the real and (b) the imaginary parts of the dielectric constant of Au and (c) the real and (d) the imaginary parts of the dielectric constant of Cu. The blue lines denote the calculation results with only intraband transitions considered, while the black lines denote the calculation results including contributions from both intraband and interband transitions. The red circles are experimental data from Ref. 27. The dashed lines indicate the positions of the ITTs.

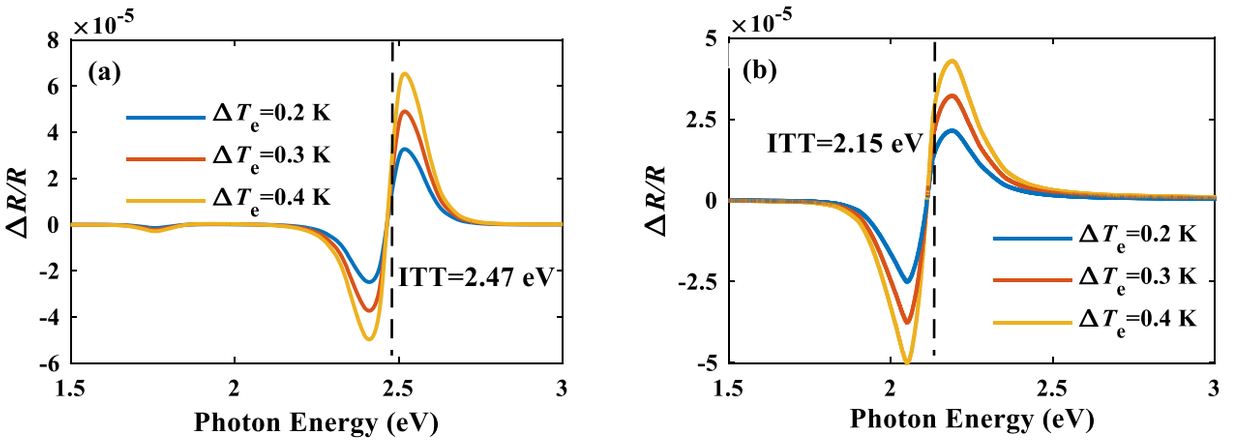

FIG. 4. Relative reflectance change of (a) Au and (b) Cu for three values of temperature changes 0.2 K, 0.3 K, and 0.4 K (initial temperature 300 K) by considering only interband transitions. The change near the ITT is mainly caused by transitions near the L point for both Au and Cu. In (a), the small change near 1.7 eV is from transitions near the X point. The dashed lines indicate the positions of the ITTs.

Ⅲ. EXPERIMENTAL STUDY OF THERMOREFLECTANCE

A. Experiment Procedure

In our experiments, Au and Cu are used as the metal thermal transducers to verify the theoretical calculation and the feasibility of the experiment system. Au and Cu with thickness of 110 nm and 120 nm respectively are coated on Si substrates with (100) surface by an E-beam evaporator. The evaporation is conducted in a vacuum chamber with a pressure less than 6.65×10^{-4} Pa.

The TDTR experiment system is shown in Fig. 5. The beam from an Yb: KGW laser (Pharos-10 W, Light Conversion) with a repetition rate of 50 kHz and a center wavelength of 1030 nm (1.2 eV) is split into a pump beam and a probe beam through a beamsplitter. The pump wavelength is tuned to and fixed at 840 nm (1.48 eV) by an OPA (Orpheus-N-2H, Light Conversion) to facilitate comparison with the TDTR signals by a Ti: sapphire femtosecond laser. The probe spectrum is tunable through another OPA (Orpheus-F, Light Conversion). The pump is modulated by a mechanical chopper at a frequency of 500 Hz. The probe is delayed temporally with respect to the pump by a motorized delay stage. The probe beam is further divided into two arms by a beamsplitter before reaching the sample in order to provide a reference signal to enable differential detection. The reflected probe beam from the sample enters a balanced detector and the differential signal is consequently detected by a lock-in amplifier with the

modulation signal of the chopper as a reference. During the data acquisition, the time constant of the lock-in amplifier is set as 300 ms. The focusing lens in front of the sample is a plano-convex lens (LA1986, Thorlabs) with focal length equal to 125 mm. In our setup, the pump and the probe beams are applied in a non-collinear configuration. The probe is perpendicular to the sample surface and the incidence angle of the pump is about 2.75°. The probe wavelength is varied from 460 nm to 730 nm (1.7 eV to 2.7 eV). The fluence of the pump is kept at 4.07 J/m^2, which causes a temperature rise of approximately 0.3 K and 0.4 K (for equilibrium between electrons and lattice) for the Au- and the Cu-Si samples, respectively. The $1/e^2$ diameter of the pump spot is 250 μm while that of the probe spot varies from 35 to 90 μm depending on the output spectrum from the OPA. Note this spectrally-tunable TDTR system is a useful platform to validate our theoretical framework since it enables the direct measurement of the thermoreflectance spectrum for a given metal transduser. The knowledge gained from this platform can also be easily transferred to a typical TDTR setup with fixed probe wavelength and high repetition rate, which might be more commonly used for specific thermal characterization.

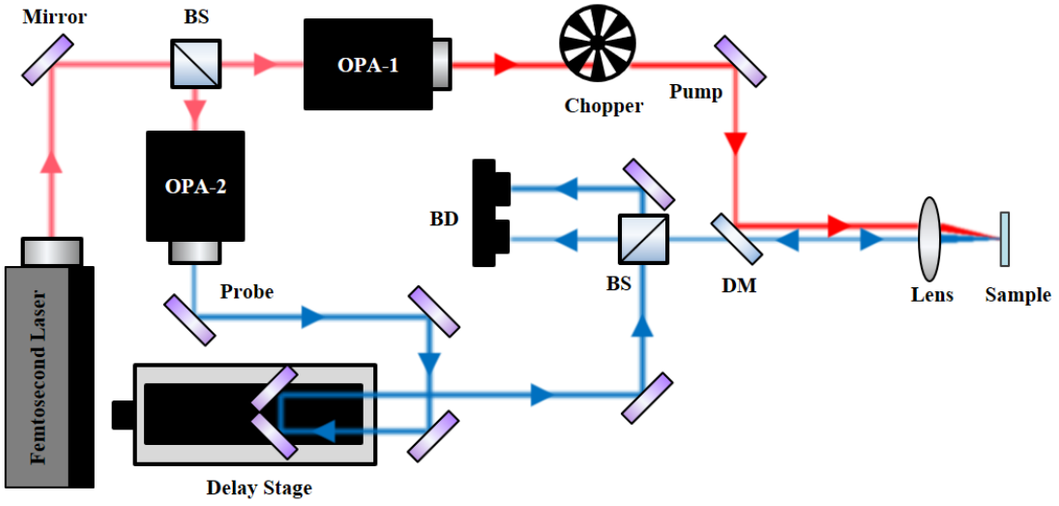

FIG. 5. Schematic of the TDTR experiment system used in this work. OPA-1 is Orpheus-N-2H for tuning the pump wavelength, and OPA-2 is Orpheus-F for tuning the probe wavelength. BS is the beamsplitter used to split one laser beam into two arms. BD denotes the balanced detector, which enables differential detection. DM is the dichroic mirror combining the pump and probe beams with different colors.

B. Results and Discussion

Figure 6(a) and 7(a) show the TDTR signals of the Au- and the Cu-Si samples with different probe photon energies, respectively. As shown, the amplitude and the sign of the TDTR signal depend strongly

on the probe photon energy even with the same heating conditions. In the measurement, each data point on the signal from one delay scan is an average of 10 data points acquired by the lock-in amplifier. And the final signal is a further average by repeating the delay scan by 6-16 times. The sign of the signal switches near the ITT. Generally, the data analysis in TDTR experiments considers data from tens of picoseconds to several nanoseconds, when electrons and lattice have reached equilibrium and the temperature evolution can be well described by Fourier's law of heat conduction. For both Au and Cu, acoustic signals appear within 250 ps featured by periodic modulation of the transient reflectance signal, which affect quantification of the signal amplitude. Therefore, we summarize the amplitudes (with sign and normalized by the maximum on the plot) at 350 ps as a function of the probe photon energy for the Au- and the Cu-Si samples in Fig. 6(b) and 7(b), respectively, together with the calculation results by the theoretical strategy discussed in Section Ⅱ. Comparing with the calculated results, the experimental results seem to be shifted. This is mainly due to the following points. First, the electronic band structure is calculated in its ground state using first-principles calculations, which is effectively at a temperature of 0 K. The assumption results in a difference between the calculated band structure and the actual band structure at a finite temperature. In addition, in the calculation, each point on the curve is the reflected signal at a single wavelength. While in the experiment, the femtosecond laser covers a certain spectral band, and the measured results are the reflected signals covering a certain range. When the photon energy is lower than the ITT, the reflectance decreases with increasing electron temperature. The reflectance change shows an opposite behavior when the photon energy is higher than the ITT. Meanwhile, the absolute amplitude of $\Delta R/R$ varies with the photon energy and reaches local extrema near, but not exactly at, the ITT. The maximum appears on the blue side of the ITT while the minimum appears on the red side.

For comparison, the amplitudes (with sign and normalized by the maximum on the plot) at the maximum/minimum value of the TDTR signal as a function of the probe photon energy are shown for the Au- and the Cu-Si samples in Fig. 6(c) and 7(c), respectively. The calculation results are also shown for comparison, for which the electron temperature is estimated by the two-temperature model considering electron-lattice nonequilibrium. Near the ITT, the TDTR signal may have opposite signs for the same probe photon energy at 350 ps and at the maximum/minimum. For example, in Fig. 6 (b) and (c), probing with 2.48 eV and 2.495 eV renders opposite signal signs at 350 ps and at the maximum/minimum. This result can be attributed to the slight change of the ITT value caused by lattice heating at 350 ps, which is absent at the maximum/minimum. The lattice heating effect, which could modify the band structure, is not included in the calculation of thermoreflectance.

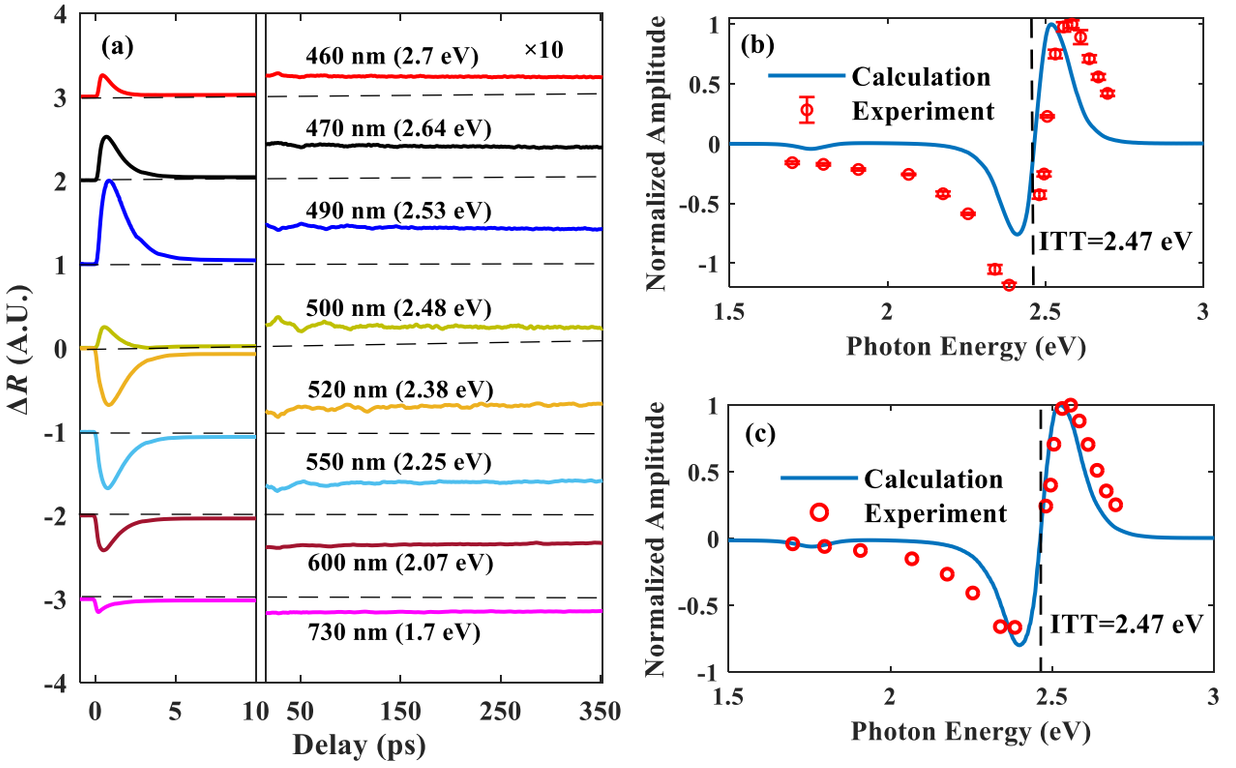

FIG. 6. (a) TDTR signals with different probe photon energies of the Au-Si sample. The signals have been multiplied by 10 in the equilibrium temporal regime (>10 ps). The curves are shifted vertically for visual clarity. The periodic modulation in the signal indicates acoustic wave, which is most distinguishable for the signal probed at 500 nm. Normalized TDTR signal amplitudes at (b) 350 ps and (c) the maximum/minimum value of the Au-Si sample. The blue curve indicates the calculation results based on the theoretical strategy in Section II and the red circles indicate the experimental data. The dashed lines indicate the positions of the ITTs.

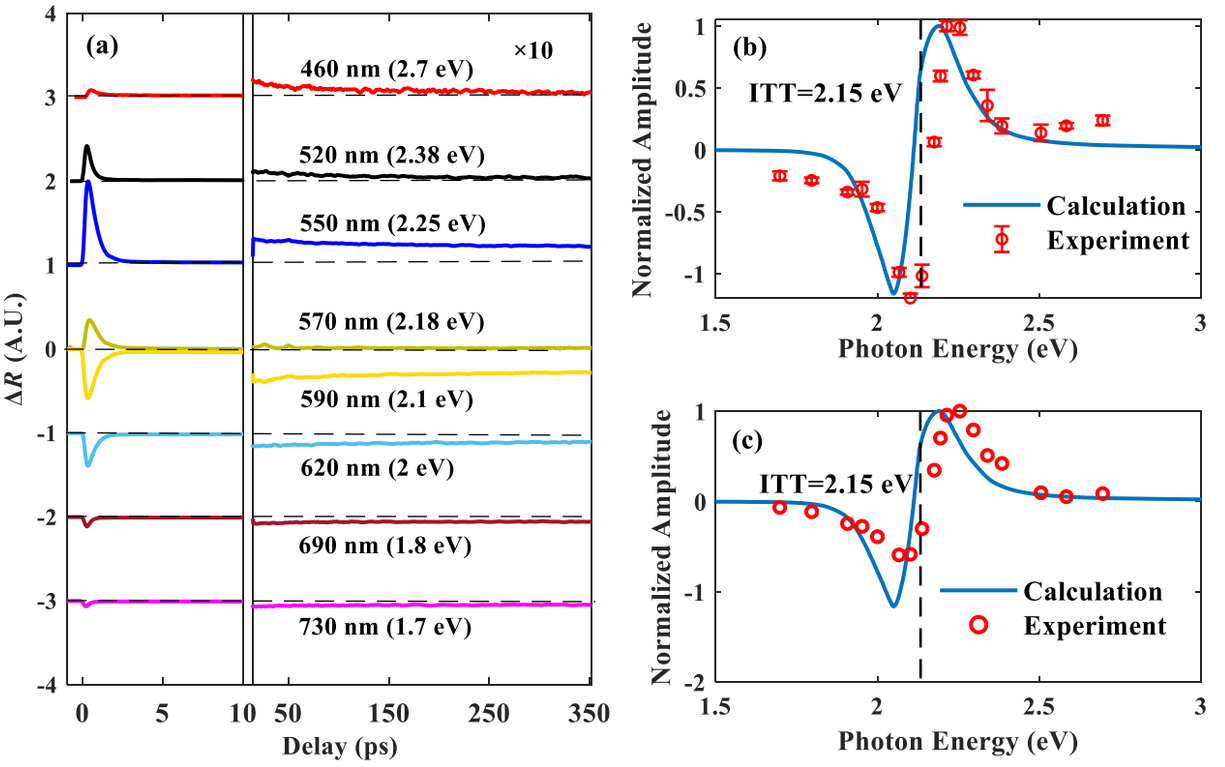

FIG. 7. (a) TDTR signals with different probe photon energies of the Cu-Si sample. The signals have been multiplied by 10 in the equilibrium temporal regime (>10 ps). The curves are shifted vertically for visual clarity. The periodic modulation in the signal indicates acoustic wave, which is most distinguishable for the signal probed at 570 nm. Normalized TDTR signal amplitudes at (b) 350 ps and (c) the maximum/minimum value of the Cu-Si sample. The blue curve indicates the calculation results based on the theoretical strategy in Section II and the red circles indicate the experimental data. The dashed lines indicate the positions of the ITTs.

The trend of the thermoreflectance spectra of metals is fundamentally explained as following. The electron occupation described by the Fermi-Dirac distribution has the largest change below and above the Fermi level while the occupation at the Fermi level remains 1/2 as temperature changes. The electron occupation change also decreases towards zero as the energy level goes far away from the Fermi level. Probing with photon energy equal to the ITT corresponds to the interband transition from the *d* band to the Fermi level in the *s*/*p* band. Therefore, the local extrema of the absorption change, described by the imaginary part of the dielectric constant, occurs on both sides of the ITT while the absorption change exactly at the ITT should be zero. The real part of the dielectric constant is correlated with the imaginary part by the Kramers-Kronig relation and also contributes to determination of the reflectance. Therefore, the zero of $\Delta R/R$ appears close to, but slightly away from, the ITT. Intraband transitions do contribute to

the dielectric constant but have much smaller contribution to the change of the dielectric constant compared with interband transitions. Therefore, probe with photon energy near (but not the same as) the ITT enables sensitive detection of temperature change by reflectance and thus the signal-to-noise ratio in TDTR measurement can be optimized by carefully selecting the probe photon energy.

IV. CONCLUSION AND OUTLOOK

In conclusion, this work presents a general approach to calculate the thermoreflectance spectra of metals, which provides a theoretical guide for matching a given metal thermal transducer with the corresponding probe photon energy in TDTR measurements to optimize the signal-to-noise ratio. TDTR experiments have been implemented to verify the prediction of the theory with the probe spectrum adjusted by an OPA. It is revealed that, given a metal as the thermal transducer, a probe with a photon energy near (but not the same as) the ITT provides high sensitivity of reflectance to temperature change and thus optimized signal-to-noise ratio in TDTR measurements. Besides Au and Cu used in this work, this framework also applies for other metals with the Fermi level in the *s*/*p* band such as Al and Ag.

In this work, spectrum tuning is realized by an OPA driven by a low-repetition rate and high-pulse energy laser. High-repetition rate (usually also low-pulse energy) lasers preferred for signal phase analysis in TDTR can be equipped with an OPO to extend the spectral range, which does not require high input pulse energy. Alternatively, self-phase modulation in nonlinear fibers can be used as an economic strategy to generate supercontinuum spectrum with a low-pulse energy femtosecond laser, from which a proper photon energy can be selected by a bandpass filter. The strategy of spectrum tuning can also be extended to TDTR or frequency-domain thermoreflectance (FDTR) realized by continuous wave lasers[28, 29].

The flexibility of selecting metal thermal transducers and the corresponding probe photon energies could first adapt TDTR to extensive experimental conditions. Particularly, metal-semiconductor junctions are key components of electronic devices and the study of the interface thermal resistance of such junctions has been a popular and challenging topic in the heat transfer community. In electronic industry, metal-semiconductor junctions may involve various metals based on the consideration of, for example, work function. The metal component in such junctions can be directly used as the thermal transducer for

measurements of the interface thermal resistance by TDTR, provided that the optimal probe photon energy is accessible. Therefore, dual selection of metal thermal transducers and probe photon energies in TDTR enables *in situ* characterization of thermal performance of electronics. In addition, the framework introduced in this work could broaden the adaptability of TDTR to various new laser sources.

ACKNOWLEDGEMENTS

This theoretical work is supported by the National Natural Science Foundation of China (51806094) and Characteristic Innovation Project of Department of Education of Guangdong Province (2018KTSCX202). This experimental work is supported by the Introduced Innovative R&D Team of Guangdong (2017ZT07C062), Centers for Mechanical Engineering Research and Education at MIT and SUSTech (Y01346002), and Shenzhen Science and Technology Program (KQTD20170810110250357).

DATA AVAILABILITY

The data that support the findings of this study are available from the corresponding author upon reasonable request.

APPENDIX

Appendix A: The calculation details of JDOS

In the band structures of Au and Cu, the *d* band and the *s*/*p* band near the high-symmetry L point and X point are approximated to be ellipsoid and hyperboloid, respectively, which are given as:

$$E_d = E_{d,0} - \frac{\hbar^2 |\boldsymbol{k}_\perp|^2}{2m_{d,\perp}} - \frac{\hbar^2 |\boldsymbol{k}_{//}|^2}{2m_{d,//}} \tag{A1}$$

$$E_{s/p} = E_{s/p,0} + \frac{\hbar^2 |\boldsymbol{k}_\perp|^2}{2m_{s/p,\perp}} - \frac{\hbar^2 |\boldsymbol{k}_{//}|^2}{2m_{s/p,//}} \tag{A2}$$

The Fermi level is set as 0 eV and $E_{d,0}$ and $E_{s/p,0}$ are defined in Fig. 2. $\boldsymbol{k}_{//}$ and $\boldsymbol{k}_\perp$ are the wave vectors in the directions from the L point (or the X point) to the Γ point and the W point, respectively. $m_{d,\perp}$, $m_{d,//}$, $m_{s/p,\perp}$ and $m_{s/p,//}$ are electron effective mass in the *d* band and the *s*/*p* band. The band parameters of Au

and Cu near the L point and the X point used in the calculation are provided in Table Ⅰ, in which m_e denotes the mass of free electrons.

The energy distribution of the JDOS (EDJDOS) is expressed as[30]:

$$D(E,\omega)=\frac{2}{(2\pi)^3}\int\frac{dl_{s/p,d}}{\left|\nabla_{\boldsymbol{k}}(E_{s/p})\times\nabla_{\boldsymbol{k}}(E_d)\right|}=\frac{2}{(2\pi)^3}\int_0^{2\pi}\frac{|\boldsymbol{k}_\perp|\,d\theta}{\left|\nabla_{\boldsymbol{k}}(E_{s/p})\times\nabla_{\boldsymbol{k}}(E_d)\right|} \tag{A3}$$

The intergral path has cylindrical symmetry about $\boldsymbol{k}_{//}$ in the reciprocal space. The gradients in the denominator are calculated based on Eqs. (A1) and (A2), which renders

$$\nabla_{\boldsymbol{k}}(E_{s/p})=\frac{\hbar^2\boldsymbol{k}_\perp}{m_{s/p,\perp}}-\frac{\hbar^2\boldsymbol{k}_{//}}{m_{s/p,//}} \tag{A4}$$

$$\nabla_{\boldsymbol{k}}(E_d)=-\frac{\hbar^2\boldsymbol{k}_\perp}{m_{d,\perp}}-\frac{\hbar^2\boldsymbol{k}_{//}}{m_{d,//}} \tag{A5}$$

$$D(E,\omega)=\frac{2}{(2\pi)^3}\int_0^{2\pi}\frac{d\theta}{(\frac{\hbar^4}{m_{s/p,\perp}m_{d,//}}+\frac{\hbar^4}{m_{s/p,\perp}m_{d,//}})|\boldsymbol{k}_{//}|} \tag{A6}$$

$\boldsymbol{k}_{//}$ can be derivated based on the relations $E = E_{s/p}$ and $\hbar\omega = E_{s/p} - E_d$, which are substituted into equations (A1) and (A2). Therefore, the EDJDOS can be further derived as:

$$\begin{aligned}D(E,\omega)&\propto[\frac{\hbar^2}{2m_{d,\perp}}(E_{s/p,0}-E)-\frac{\hbar^2}{2m_{s/p,\perp}}(E-\hbar\omega-E_{d,0})]^{-0.5}\\&\propto(\frac{m_{s/p,\perp}}{m_{d,\perp}+m_{s/p,\perp}}\hbar\omega+\frac{m_{s/p,\perp}E_{d,0}+m_{d,\perp}E_{s/p,0}}{m_{d,\perp}+m_{s/p,\perp}}-E)^{-0.5}\end{aligned} \tag{A7}$$

It is necessary to provide the lower and the upper limits of the integral with respect to energy for evaluating the JDOS due to the existence of singular point.

$$\begin{aligned}E_{max}(\omega)&=[E_{s/p,0}+\frac{m_{d,//}}{(m_{s/p,//}-m_{d,//})}(E_g-\hbar\omega)]H(E_g-\hbar\omega)\\&+(\frac{m_{s/p,\perp}}{m_{s/p,\perp}+m_{d,\perp}}\hbar\omega+\frac{m_{s/p,\perp}E_{d,0}+m_{d,\perp}E_{s/p,0}}{m_{s/p,\perp}+m_{d,\perp}})H(\hbar\omega-E_g)\end{aligned} \tag{A8}$$

$$E_{min}=-5\ \text{eV} \tag{A9}$$

where $E_g = E_{s/p,0} - E_{d,0}$ and $H(x)$ is the Heaviside function. The ratio of contribution from X point to that from L point is 0.6 for Au and 0 for Cu by fitting with the measured dielectric constant.

TABLE Ⅰ. The band parameters of Au and Cu near the L point and the X point used in the calculation

		$E_{d,0}$(eV)	$m_{d,//}/m_e$	$m_{d,\perp}/m_e$	$E_{s/p,0}$(eV)	$m_{s/p,//}/m_e$	$m_{s/p,\perp}/m_e$
Au	L point	-2.2944	0.813	0.869	-0.7167	0.2535	0.2219
	X point	-1.58	1.0282	0.7017	1.5242	0.1206	0.2410
Cu	L point	-1.688	0.1886	0.2096	-0.802	0.1557	0.1343
	X point	-1.435	0.5114	0.1475	1.519	0.3445	0.1129

In this work, the band structures of Au and Cu were expressed as analytical formulas. While the band structure parameters of Au are well known, first-principles calculation was carried out for extracting the band structure parameters of Cu using the projector-augmented wave (PAW) method as implemented in the VASP code and the generalized gradient approximation (GGA) to model exchange-correlation energy functionals[31, 32]. We used a uniform Monkhorst-Pack scheme grid consisting of 32×32×32 ***k***-points in the first Brillouin zone with an energy cut-off of 400 eV. For metals with more complicated band structure, first-principles calculation can be performed and the JDOS can be numerically calculated. Also, the contribution to the dielectric constant from interband transitions is generally dominated by high-symmetry points in the reciprocal space, which requires only evaluation of the local band structure. Therefore, extraction of the effective masses from the band structure and using the parameters for analytical analysis are suitable for other metals.

Appendix B: The contribution of intraband transitions to reflectance change

Figure 8 compares that the change of dielectric constant contributed by intraband and interband transitions in Au (0.3 K electron temperature change) and Cu (0.4 K electron temperature change). Based on the values of the proportion coefficients in Eq. (8) extracted from literature, the contribution from intraband transitions can be comparable to or even larger than the contribution from interband transitions. However, the calculated relative reflectance change $\Delta R/R$ considering both intraband and interband transitions becomes highly deviated from the experimental results in Section III as illustrated by Fig. 9. Therefore, we do not think the values cited in Eq. 8 are appropriate to evaluate the influence of temperature

on reflectance from the contribution of intraband transitions. According to the results presented in Section III, inclusion of interband transitions alone can well fit the experimental results, implying the thermally-induced reflectance change is dominated by the change of probability of interband transitions.

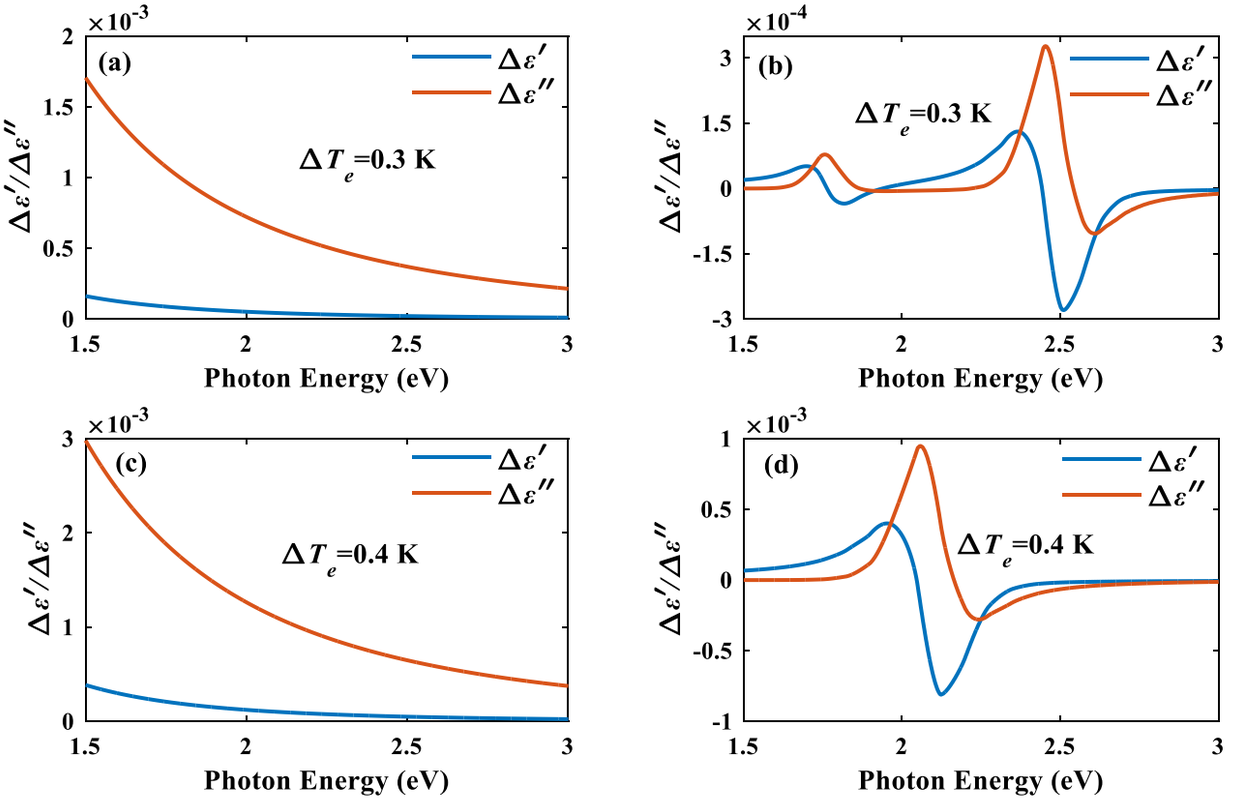

FIG. 8. The calculation results of the temperature influence on the dielectric constant from the contribution of (a) intraband transitions and (b) interband transitions of Au and the temperature influence on the dielectric constant from the contribution of (c) intraband transitions and (d) interband transitions of Cu. The blue lines indicate the changes of the real part of the dielectric constant, while the red lines indicate the changes of the imaginary part of the dielectric constant. The temperature change is 0.3 K for Au and 0.4 K for Cu (initial temperature 300 K).

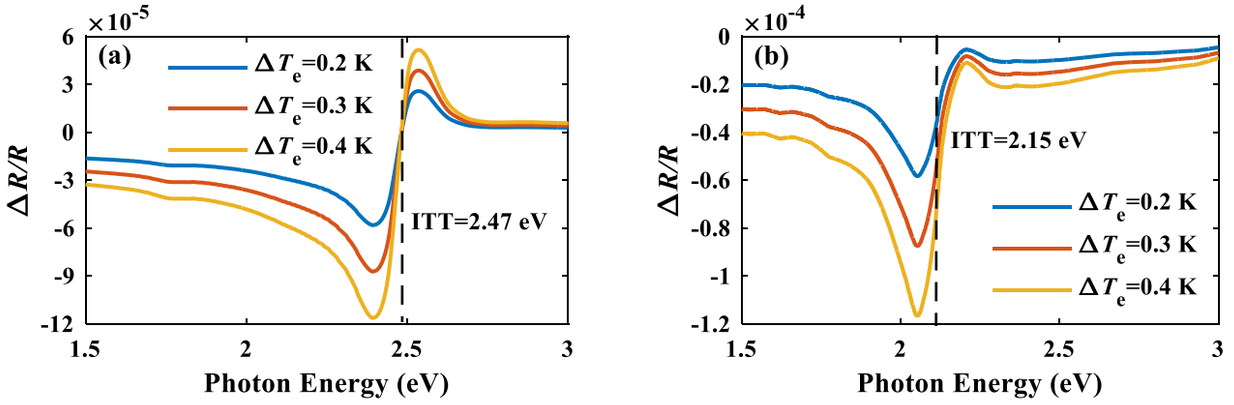

FIG. 9. The relative reflectance change of (a) Au and (b) Cu for three values of temperature changes 0.2 K, 0.3 K, and 0.4 K (initial temperature 300 K) by considering both intraband transitions and interband transitions. The dashed lines indicate the positions of the ITTs.

REFERENCES

[1]S. Narayana and Y. Sato, Phys. Rev. Lett. 108 (21), 214303 (2012).

[2]L. D. Zhao, S. H. Lo, Y. Zhang, H. Sun, G. Tan, C. Uher, C. Wolverton, V. P. Dravid, and M. G. Kanatzidis, Nature 508, 373–377 (2014).

[3]Q. Y. Li, W. G. Ma, and X. Zhang, Int. J. Heat Mass Tran. 95, 956-963 (2016).

[4]H. Wang, S. Hu, K. Takahashi, X. Zhang, H. Takamatsu, and J. Chen, Nat. Commun. 8, 15843 (2017).

[5]K. C. Collins, A. A. Maznev, J. Cuffe, K. A. Nelson, and G. Chen, Rev. Sci. Instrum. 85, 124903 (2014).

[6]Y. Choi, D. Jeong, H. I. Ju, C. J. Roh, G. Kim, B. S. Mun, T. Y. Kim, S. Kim, J. S. Lee, Sci. Rep. 9, 7612 (2019).

[7]J. S. Kang, M. Li, H. Wu, H. Nguyen, and Y. Hu, Science 361, 575-578 (2018).

[8]S. Li, Q. Zheng, Y. Lv, X. Liu, X. Wang, P. Y. Huang, D. G. Cahill, and B. Lv, Science 361, 579–581 (2018).

[9]Y. Xu, D. Kraemer, B. Song, J. Zhang, J. Zhou, J. Loomis, J. Wang, M. Li, H. Ghasemi, X. Huang, X. Li, and G. Chen, Nat. Commun. 10, 1771 (2019).

[10]B. Sun, G. Haunschild, C. Polanco, J. Ju, L. Lindsay, G. Koblmuller, and Y. K. Koh, Nat. Mater. 18, 136-140 (2019).

[11]R. Rosei and D. W. Lynch, Phys. Rev. B 5, 3883-3894 (1972).

[12]J. H. Weaver, D. W. Lynch, C. H. Culp, and R. Rosei, Phys. Rev. B 14, 459-463 (1976).

[13]R. B. Wilson, B. A. Apgar, L. W. Martin, and D. G. Cahill, Opt. Exp. 20(27), 28829-28838 (2012).

[14]J. J. Gengler, S. Roy, J. G. Jones, and J. R. Gord, Meas. Sci. Technol. 23, 055205 (2012).

[15]H. E. Elsayed-Ali, T. B. Norris, M. A. Pessot, and G. A. Mourou, Phys. Rev. Lett. 58(12), 1212-1215 (1987).

[16]R. W. Schoenlein, W. Z. Lin, J. G. Fujimoto and G. L. Eesley, Phys. Rev. Lett. 58(16), 1680-1683 (1987).

[17]S. A. Maier, Plasmonics: Fundamentals and Applications (Springer, 2006), pp. 11-15.

[18]M. Fox, Optical Properties of Solids (Oxford University Press, 2010), pp. 148-153.

[19]E. J. Zeman and G. C. Schatz, J. Phys. Chem. 91, 634-643 (1987).

[20]L. Guo, S. T. Hodson, T. S. Fisher, and X. Xu, J. Heat Transf. 134, 042402 (2012).

[21]P. B. Johnson and R. W. Christy, Phys. Rev. B 11, 1315-1323 (1975).

[22]Y. Y. Peter and C. Manuel, Fundamentals of Semiconductors (Springer, 2010), pp. 261-262.

[23]C. Kittel, Introduction to Solid State Physics (Wiley, 2004), pp. 429-433.

[24]J. Hohlfeld, S.S. Wellershoff, J. Gudde, U. Conrad, V. Jahnke, and E. Matthias, Chem. Phys. 251, 237-258 (2000).

[25]P. E. Hopkins, J. C. Duda, R. N. Salaway, J. L. Smoyer, and P. M. Norris, Nanosc. Microsc. Therm. 12, 320-333 (2008).

[26]T. Heilpern, M. Manjare, A. O. Govorov, G. P. Wiederrecht, S. K. Gray, and H. Harutyunyan, Nat. Commun. 9, 1853 (2018).

[27]P. B. Johnson and R. W. Christy, Phys. Rev. B 6, 4370-4379 (1972).

[28]J. W. Pomeroy, R. B. Simon, H. Sun, D. Francis, F. Faili, D. J. Twichen, and M. Kuball, IEEE Electron Device Lett. 35, 1007-1009 (2014).

[29]A. J. Schmidt, R. Cheaito, and M. Chiesa, Rev. Sci. Instrum. 80, 094901 (2009).

[30]R. Rosei, F. Antonangeli, and U. M. Grassano, Surf. Sci. 37, 689-699 (1973).

[31]G. Kresse and J. Furthmüller, Phys. Rev. B 54, 11169-11186 (1996).

[32]G. Kresse and J. Furthmüller, Comput. Mater. Sci. 6, 15-50 (1996).